Engineering Structures 168 (2018) 544–558

Contents lists available at ScienceDirect

Engineering Structures

journal homepage: www.elsevier.com/locate/engstruct

Dynamic response of a damaged masonry rail viaduct: Measurement and interpretation

Sinan Acikgoz[d,*], Matthew J. DeJong[b], Cedric Kechavarzi[a], Kenichi Soga[c]

[a] Centre for Smart Infrastructure and Construction, University of Cambridge, United Kingdom
[b] Department of Engineering, University of Cambridge, United Kingdom
[c] University of California, Berkeley, United States
[d] Department of Engineering Science, University of Oxford, United Kingdom

ARTICLE INFO

Keywords:
Masonry rail bridge
Fibre Bragg grating
Digital image correlation
Structural health monitoring

ABSTRACT

Despite recent advances in modelling and testing techniques, assessing the serviceability of ageing masonry rail bridges remains a significant challenge. Most assessment methods are based on ultimate strength, while reliable measurement-based assessment criteria are lacking. This paper aims to improve the understanding of serviceability behaviour through detailed dynamic monitoring of the bridge locally (e.g. in locations of damage) and globally (e.g. interaction of different components). Quasi distributed sensing techniques (Fibre Bragg Grating cables and Digital Image Correlation) were used to quantify the bridge dynamic response through extensive measurement of strains and displacements. Specifically, these techniques were applied to two damaged spans of the Marsh Lane viaduct in Leeds, UK. A detailed investigation of the dynamic pier and arch barrel movements reveal how the response mechanisms relate to, and likely propagate, the existing damage. For instance, rotation of piers in the bridge longitudinal plane causes significant span opening and closing, which in turn causes the skewbacks and backing to rock on the piers. This is accompanied by flexural deformation of the arch, which forces the existing transverse cracks to experience high compressive strains. Similarly, the transverse rotation of piers due to the presence of the relieving arches causes spreading of the relieving arches and opening of the longitudinal crack above. These observations provide new insight into behaviour and lead to suggestions for improving assessment techniques for masonry viaducts.

1. Introduction

In the last decades, passenger and freight numbers have been rapidly increasing on the European rail network [1]. In the UK, this has been accompanied by a 20% increase in the axle weight of modern vehicles and an increase in maximum line speeds on some railway routes [2]. Increased loading demands requires re-assessment, which can be a complicated task for ageing rail infrastructure. For instance, masonry arch bridges constitute 60% of the European bridge stock [3]. Most masonry bridges were constructed before the 20th century, and were not designed to sustain the increased loading that has occurred. Therefore, the engineering community have focused on developing reliable methods to determine the ultimate load carrying capacity of masonry arch bridges. These studies provide valuable understanding of the complex mechanical behaviour of masonry bridges (see [4] and the references therein). Importantly, they distinguish between the behaviour of single span arch bridges and arched viaducts with multiple spans [5]. They also establish that the limiting failure mechanism under static loading, and hence the capacity of a masonry viaduct, involves the interaction of two or more spans [6]. Other research has demonstrated the significant influence of arch backing [7], ring separation [8] and the presence of spandrel walls [9] on load carrying capacity.

However, most masonry bridges experience progressive damage for service loading well below their predicted ultimate capacity [10]. This causes their safety to be questioned as further damage and material degradation, which can occur due to cyclic environmental or dynamic loading, can decrease the load resistance. Accurately predicting the progressive damage for masonry bridges would require replicating the effects of the loading history, modelling the existing damage and simulating the dynamic response of the damaged structure to further cyclic loads with appropriate degradation models. However, significant uncertainties exist in identifying typical sources and propagation of damage observed in masonry arch rail bridges. These uncertainties limit the ability of uncalibrated computational models to capture critical progressive damage mechanisms.

To advance the current understanding of the serviceability response

* Corresponding author at: Department of Engineering Science, University of Oxford, 15 Parks Road, OX1 3PJ.
E-mail address: sinan.acikgoz@eng.ox.ac.uk (S. Acikgoz).

https://doi.org/10.1016/j.engstruct.2018.04.054
Received 4 September 2017; Received in revised form 10 April 2018; Accepted 16 April 2018
Available online 09 May 2018

of masonry bridges, field measurements to quantify the current damage state of the structure are essential. In recent years, useful non-contact methods have been developed to achieve this [11–15]. These include (a) ultrasound testing to determine the surface material characteristics, (b) ground penetrating radar surveys to determine the interior structure and (c) laser scan surveys to determine the current distorted geometry of the structure. These techniques, alongside traditional measurements such as crack measurement and hammer tapping, provide important information regarding the damage state of the existing asset.

For assessments, it is equally important to capture the dynamic response of the structure to cyclic loads and document its degradation process. Traditional monitoring tools, such as displacement gauges, tiltmetres, strain gauges and accelerometers, are typically used for this purpose [16–20]. However, these techniques capture the local behaviour of the material and are difficult to interpret without multiple measurements at different locations [21]. In contrast, quasi-distributed monitoring techniques, such as sensing with Fibre Bragg Gratings (FBGs) and digital image correlation (DIC), make it feasible to obtain strain and displacement measurements across wide areas of the structure. Direct strain and displacement measurement is useful because visible damage in a masonry arch may not always quantify the active degradation processes. Further, distributed techniques enable local measurements around locations of damage (e.g. cracks), as well as global displacement measurements (e.g. span opening and closing) simultaneously. Useful quantities, such as rotation and crack opening, can be determined by post-processing, in order to identify the governing response mechanisms.

This paper describes a novel application of the aforementioned quasi-distributed techniques for monitoring a masonry viaduct and demonstrates the understanding of structural response that can be obtained from a comprehensive monitoring programme. To do this, two spans of the Marsh Lane Viaduct in Leeds, UK, are investigated. The structure, the observed damage, the monitoring installation, and the data processing are first discussed, followed by the interpretation of measurements to understand the complex three-dimensional dynamic behaviour. The response to a typical passenger train is examined in detail, followed by the investigation of the bridge response to different vehicles and evaluation of degradation over a six month monitoring interval.

2. The investigated structure

Marsh Lane viaduct is a masonry viaduct on the Leeds-Selby route (see Fig. 1a). The investigated section, which comprises of Arches 37 and 38, was constructed during the North Eastern Railway Leeds Extension between 1865 and 1869 [22]. The bridge carries two electrified tracks, and has a speed limit of 35 mph.

The plan view of the viaduct in Fig. 1a shows that the investigated arches are on a gently curving section of the railway. At the location of arches 37 and 38, the curvature is primarily achieved by varying the pier thicknesses by approximately 0.25 m across the bridge width. The average pier thickness is approximately 0.85 m. It is noteworthy that the piers are not completely solid. Relieving arches consisting of 3 rings and spanning 2.5 m lies in the middle of the piers. This relieving arch is visible in the photo in Fig. 1b, which was taken in July 2015. Fig. 2, a photo taken shortly after the remedial works in September 2015, shows the same arch filled with concrete.

Table 1 lists the key dimensions of Arches 37 and 38. The height of the brick piers from the ground level is measured as 2.7 m, although the foundations of the bridge run deeper. During the remedial works, it was observed that the relieving arch has a mirror image invert beneath the current ground level and a corbelled foundation underneath. Assuming that the invert lies just under the ground level with a 0.5 m foundation underneath, suggests that the total pier height from the bottom of the foundation is approximately 5.2 m. The construction of the arch above its pier is shown on the right side of Table 1. Both investigated arches have an approximate span of 7.7 m and a width of 8 m. According to this schematic, a series of large skewback stones, approximately 0.6 m high, were placed above the pier, along the width of the bridge. The primary arch barrels have 4 rings with a total thickness of ~0.5 m and a rise of 1.8 m. Just above the skewback, there is evidence of a 1.15 m layer of backing, including the coinciding presence of drainage holes and horizontal cracking on the spandrel wall. Above the backing, a layer of compacted earth fill supports the ballasted tracks, and is contained from both sides by 0.5 m thick spandrel walls. Further information was not available on the properties of materials used in the construction of the bridge.

The side photo of the bridge in Fig. 2 highlights visible structural damage as well as the related structural interventions. The photo shows the north-facing spandrel wall of Arch 38, where significant damage has concentrated. The damage includes horizontal cracks on the spandrel wall, which appear due to higher flexural stiffness of the spandrel wall in comparison to the arch barrel [7]. There is also evidence of partial separation between the spandrel wall and the extrados of the arch (Fig. 2). These damages have led to repointing on the western side of the 38N spandrel wall. Signs of damage and interventions can also be observed on the piers. In particular, water drainage issues have affected the western pier of Arch 38, which has been repointed. In addition, the significant use of steel ties can be observed. In the 1990s, ties were installed through the arch barrel to limit further opening of longitudinal barrel cracks. In September 2015, several other ties were installed; ties on the piers were located close to the ground level, to arrest transverse movements of the piers, whereas the ties on the spandrel walls aimed to prevent bulging.

Damage visible from the underside of Arch 38 is discussed with annotated photos in Fig. 3. In particular, the significant movements and

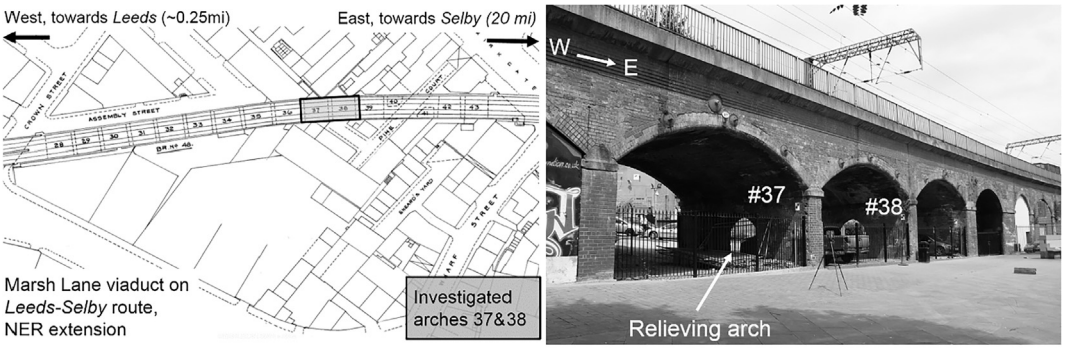

Fig. 1. (Left) Plan view drawing of a section of the Marsh Lane viaduct (British Railways drawing 73-YWR-513) and (Right) a photo showing the southern side view of the investigated arches 37 and 38.

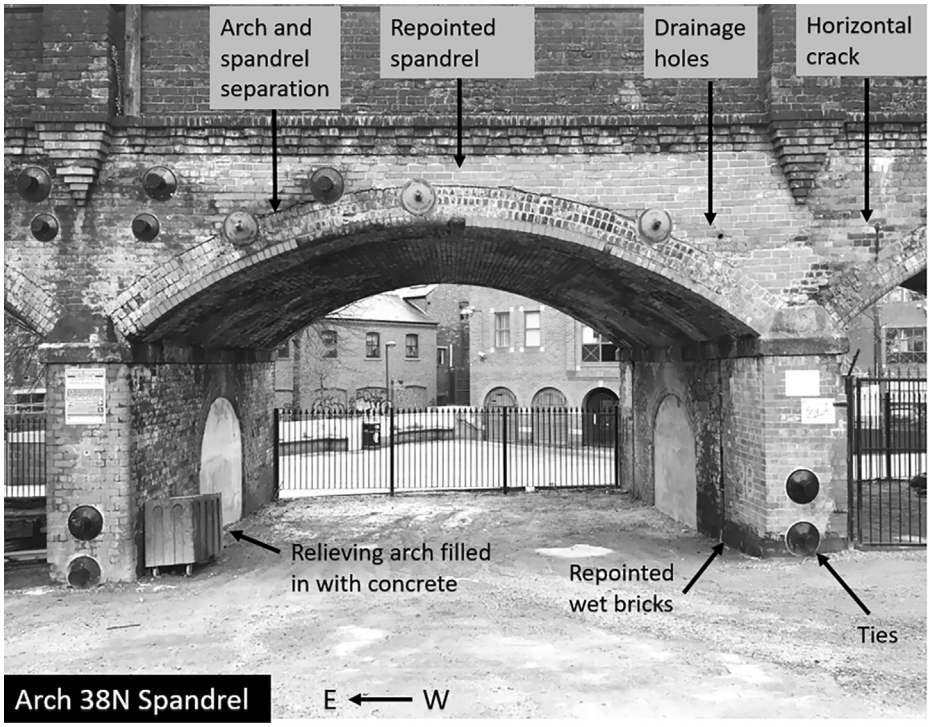

Fig. 2. A photo showing the northern side view of Arch 38. Annotated boxes draw attention to signs of structure damage and related maintenance works.

Table 1
A summary of the key characteristics of the tracks on the Marsh Lane viaduct alongside geometric characteristics of the investigated Arch 38.

Structure	Route	RA number	Number of tracks	Speed limit (mph)
Marsh Lane viaduct	Leeds-Selby	10	2	35
Structure	Bridge Span (m)	Bridge Rise (m)	Bridge Width (m)	Arch thickness (m)
Arch 38	7.7	1.8	8	0.5
	Skewback height (m)	Backing Height (m)	Pier thickness (m)	Estimated pier height (m)
Arch 38	0.6	1.15	0.85, varying	5.2

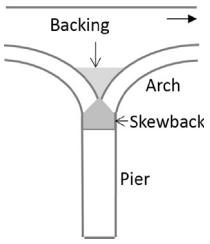

rotations observed in the western pier are shown in Fig. 3b. The skewback stones decline in elevation on both sides of the relieving arch, reaching a minimum elevation just above the crown, indicating a spreading mechanism in the relieving arch. This mechanism is accompanied by visible cracking of the relieving arch around its crown and significant openings between the skewback stones. The transverse rotation of pier bricks below and above the springing of the relieving arch (illustrated in Fig. 3b) also relate to this mechanism. It is likely that the spreading mechanism and transverse pier rotations are due to the load path which imparts considerable vertical live loads on the relieving arch. The relieving arch then thrusts on the piers in the bridge transverse direction, causing them to rotate towards the spandrel walls. As mentioned earlier, the relieving arch was filled with concrete in September 2015.

The relieving arch spreading mechanism caused damage in the arch barrel, which is shown in Fig. 3a. For instance, in the western side of Arch 38, a longitudinal crack which emanates from the relieving arch is visible. This crack is due to the rotation of the northern pier towards the northern spandrel wall (see Fig. 3b). The crack is 3 cm wide at the arch springing and reduces to a hairline crack at the quarter span. It is interesting that the crack does not follow a straight line but branches out in two directions. During the September 2015 repair works, all of these cracks were grouted and stitched. However, by July 2016, hairline cracks appeared through the grout, suggesting that the repair works may not have arrested the transverse separation movement of the piers completely. Two other noteworthy signs of damage were observed for Arch 38 in Fig. 3a. The first relates to rounding and cracking of skewback stones at their edges along the bridge longitudinal direction. Prior to repair works, it was noticed that these stones rotate visibly on piers in the bridge longitudinal direction during the passage of trains [23]. The other significant damage that was observed relates to transverse cracking of the arch barrel just above the backing of the pier between Arches 37 and 38, and related water ingress. In-depth analysis of bridge geometry from laser scan surveys indicated that the cracking was in response to the aforementioned spreading and vertical depression of the relieving arch between Arches 37 and 38 [15]. The schematics in Fig. 3c summarise the damage observed on the western pier of Arch 38 and arch barrel intrados of Arches 37 and 38 and emphasise widespread nature of existing damage. In order to determine the response mechanism of the bridge and understand the causes of degradation, monitoring the response of the structure in many different locations was necessary.

3. Monitoring techniques

This section describes the application of the FBG and DIC sensing techniques, which were used to monitor Arches 37 and 38. FBG technology utilises a Germanium doped single mode silica fibre. The fibre is

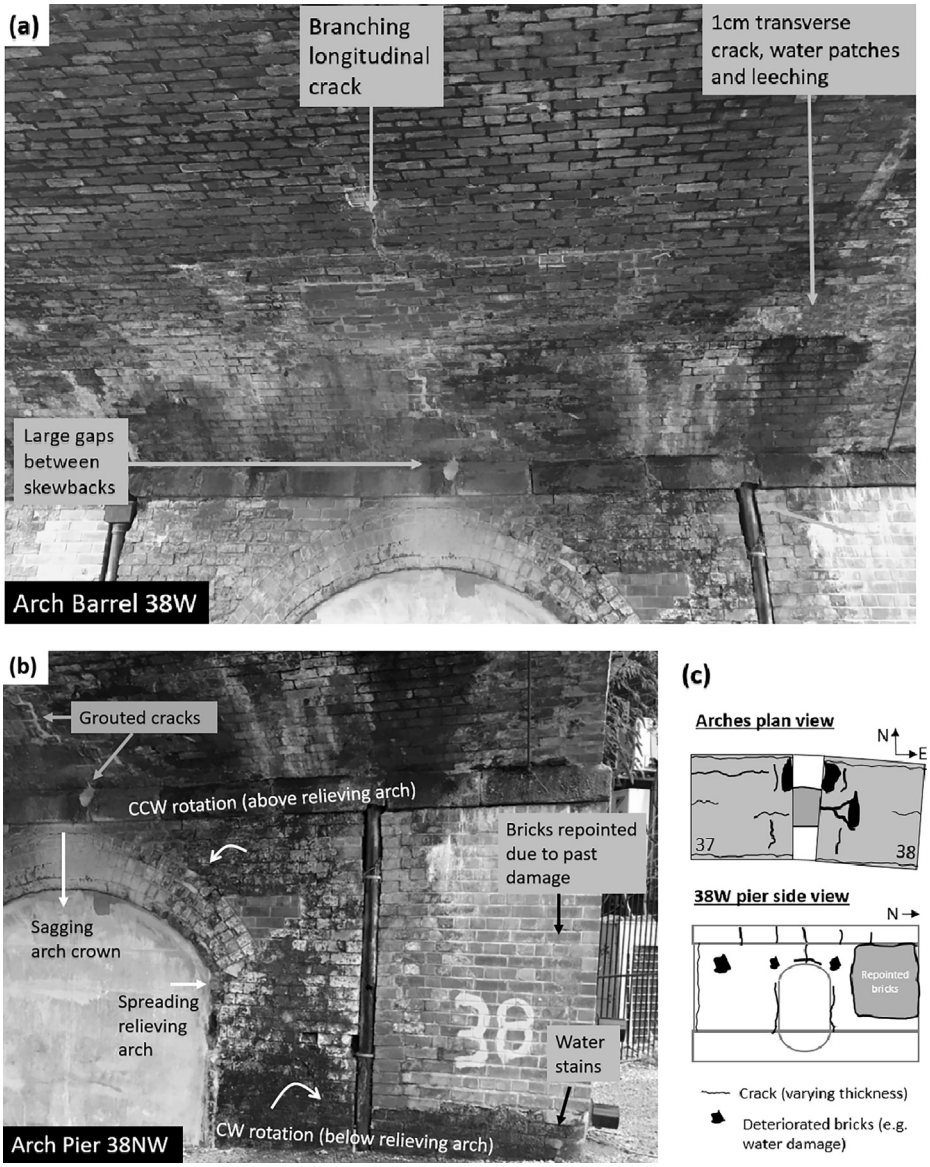

Fig. 3. Annotated photos of (a) the western part of the arch barrel 38 and (b) the pier on the northwest side of the same arch. (c) The observed damage is summarised with the schematic drawings of Arches 37 and 38.

subjected to ultraviolet light with a phase mask to create gratings (areas with modified refractive index) on the cable. When a light pulse is sent into the fibre, each grating reflects the light at a particular wavelength λ_0 while transmitting the rest of the signal. This backscatter central wavelength, denoted by λ, is sensitive to changes in temperature and strain [24]. Since only transient dynamic data is investigated, the influence of temperature changes on the wavelength data is negligible. Therefore, observed changes in wavelength $\Delta\lambda = \lambda - \lambda_0$ can be used to calculate changes in axial strain $\Delta\varepsilon$ as follows:

$$\Delta\varepsilon = \frac{\Delta\lambda}{\lambda_0(1-\rho_e)} \tag{1}$$

where the constant $\rho_e = 0.23$, and is defined as the effective photo-elastic constant of the fibre core material and was determined through calibration tests at the laboratory.

Six custom designed arrays of fibre optic cable with 120 gratings were used to detect the axial strains on the masonry structure (Fig. 4a). Each array featured a fibre optic cable with twenty low reflectivity (< 20%) gratings, placed 1 m apart. Each grating on the fibre had a central wavelength which differed from the next grating by 4 nm, guaranteeing a strain measurement range of ± 1500$\mu\varepsilon$. To ensure that the fibre was robust enough for external use, a new fibre configuration was developed in collaboration with the manufacturer (FBGS International NV, Geel, Belgium). The 125 μm core of this fibre consisted of a 6 μm inner core with a high reflective index, surrounded by an outer core of glass, with a lower reflective index. The core is coated with organic modified ceramic to prevent water ingress. The external layers of Glass-Fibre Reinforced Polymer (1 mm thick) and High Density Polymer (0.5 mm thick) provide stiffness and further protection against elements. The fibre was spliced to a standard telecom extension cable, to route the cables to a monitoring location under the arches, (see Fig. 4b). The central wavelengths of gratings in each array were kept in the 1510–1590 nm range, which defines the bandwidth of the Micron-Optics sm-130 fibre optic interrogator. A fibre optic multiplexer was used to near-simultaneously record the strains in 120 FBGs at a sampling rate of 250 Hz. The sensing system could achieve a strain resolution of 1 $\mu\varepsilon$. The fibre optic cable was fixed on the bricks using precision machined aluminium clamps, typically placed 1 m apart. The fibre was prestrained to approximately 500 $\mu\varepsilon$, to detect compression as well as tension.

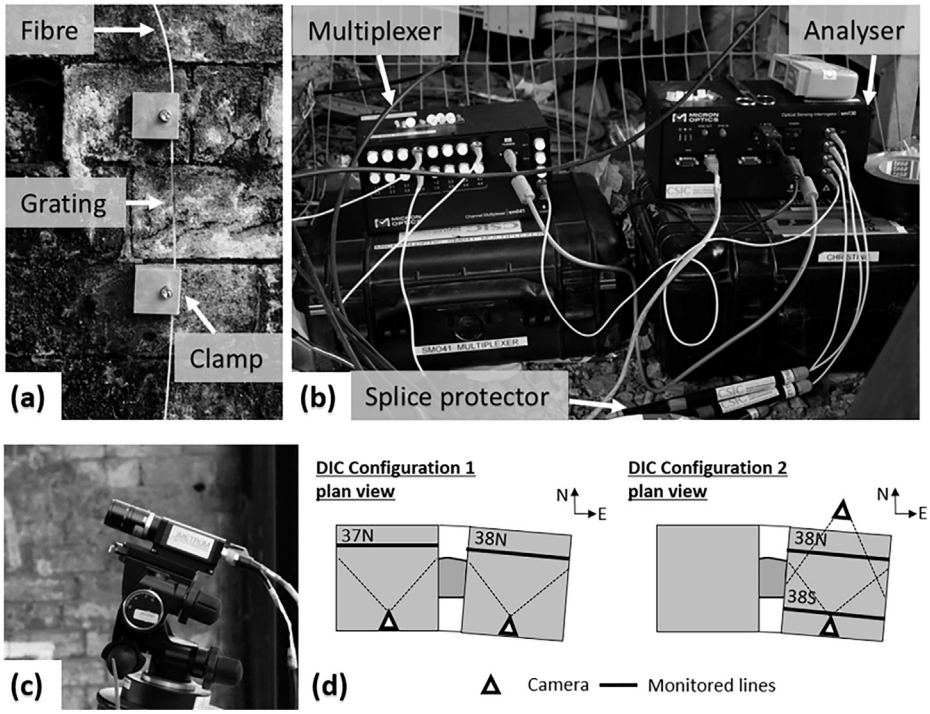

Fig. 4. Photos of (a) the installed fibre optic cable and clamps, (b) the fibre optic analyser with a multiplexer and (c) the Imetrum video camera. The schematics (d) demonstrate the location configurations of the video cameras for digital image correlation.

A commercial DIC system (Imetrum Ltd., Bristol, UK) was used to monitor the displacements of the viaduct. This system complemented the fibre optic system, as it could be used to estimate rigid body rotations of masonry arch segments. The DIC system consisted of two video cameras and a system controller (see Fig. 4c). The cameras recorded videos of the monitored structure at a 50 Hz frame rate. Data processing consisted of tracking the sub-pixel position of natural brick texture in the image, accomplished using the Imetrum software, and scaling of pixel movements to metric movements with the use of a new registration technique proposed by the authors [25]. In order to understand the viaduct behaviour, two different camera location configurations, which are presented in Fig. 4d, were investigated with 2D DIC. In the first configuration C1, the cameras monitored planar movements of Arches 37 and 38 in the vertical plane directly under the northern tracks, aligned with the bridge longitudinal axis. These planes correspond to unique XY planes, referred to as 37N and 38N. In the second configuration C2, the cameras monitored the movements in the vertical planes lying under the northern and southern tracks of Arch 38 along the bridge longitudinal axis, respectively referred to as 38N and 38S. In both configurations, the cameras were positioned centrally in line with the crown of the arches. This setup allowed capturing all the targets with a 0.08 mm resolution in each plane from a single position.

The FBG monitoring lines were used to monitor the strains in the same planes investigated by DIC. A photo of one of these planes, 38S, is shown in Fig. 5a. In this figure, the annotations show the locations of pier monitoring targets WP and EP and arch monitoring targets A1-A9. A similar arrangement was used for monitoring the other longitudinal planes on 38N, 37N and 38S (see Fig. 5b). In this arrangement, FBG sensors measured the strains between consecutive locations, such as A1-A2 and WP-EP, while the 2D DIC technique, from which data was collected at the same locations, measured the absolute displacement of targets in the horizontal direction X and vertical direction Y. These absolute displacements were used to calculate relative displacements, to obtain the strain. The discrepancy between corresponding FBG and DIC relative displacement (strain) measurements were largely due to out of plane movements which affected DIC measurements. With a new algorithm, the out-of-plane effects were quantified and removed from DIC measurements [25]. The corrected DIC monitoring data in the XY coordinate plane, and the estimated transverse movement data in the Z direction, are presented in this paper. In relation, FBG sensors were used to measure strains in the transverse direction of the bridge. Two transverse monitoring lines were located at approximately the quarter spans of each arch, as illustrated on the right side of Fig. 5b. In Arch 38, the transverse monitoring line 38W features 7 clamps (T1-T7); strains are measured between each clamp. For instance, T2-T3 measured transverse strain under the tracks, whereas T4-T5 measured strain over the tip of the longitudinal crack.

A pilot installation of the fibre optic sensors in Arch 37 was done in January 2016. These sensors were left in place and more fibre optic sensors were installed in Arch 38 in July 2016, where the DIC system was also used. DIC and FBG systems independently gathered data, and were synchronised later by best-matching the time stamps of peaks of the common measurement of span opening and closing at the pier top, denoted by Δ(WP−EP). The synchronised measurements were related to the position of axles using videos of the train on the viaduct.

To investigate the structural response, loading information is necessary. Several different trains use the Leeds-Selby line, most notably British Rail Class 185, 155 and 144 trains. The characteristics of these trains are examined in Fig. 6. Class 185 is a diesel multiple unit vehicle with a wide wheelbase. The distance between the two bogie centres in each carriage is 16 m, which is approximately double the distance between consecutive pier centrelines d_{cr} of the investigated arches. Therefore, the normalised wheelbase is approximately 2. A typical bogie weight is 33 tons. The additional passenger weights are typically negligible compared to the train weight. Class 155 trains have similar dimensions as class 185 trains, but each bogie weighs approximately 40% less. Class 144 trains were converted in the 1980 s from disused buses. The distance between the front and back axles of each carriage is 9 m, which is approximately equal to the distance between consecutive pier centrelines, approximately corresponding to a wheelbase of 1. In addition, Class 144 trains weigh approximately one third of the Class 185 trains.

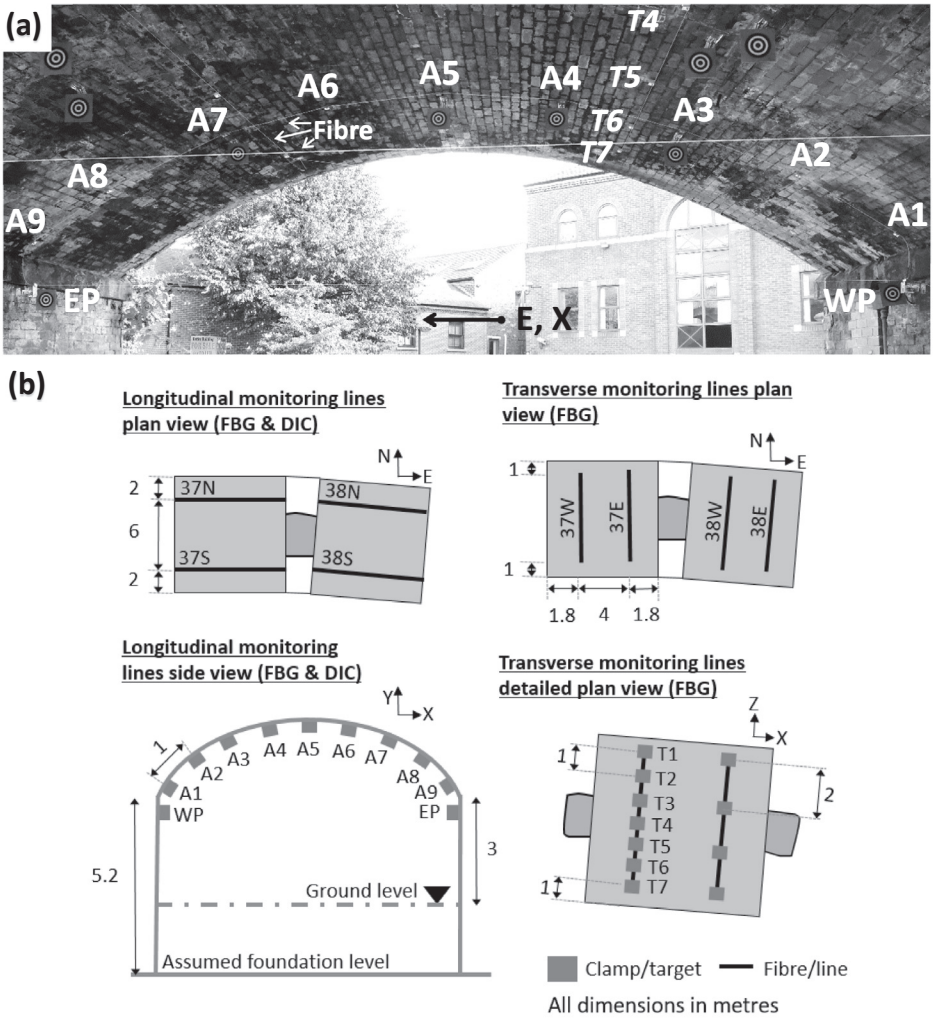

Fig. 5. (a) A south looking photo showing a side view of the longitudinal monitoring plane 38S. The annotations denote the unique ID for each clamp, where fibre optic cables are fixed and DIC tracks the natural brick and mortar pattern. (b) Schematics outline the approximate location of all monitoring lines and clamps.

As examined in [25], the train response data was quasi-static; dynamic effects were minimal. Therefore, it is possible to normalise the time data with the speed v of each train (determined from peak locations and known train distances) and d_{cr} of the investigated span. Investigating the data plotted against normalised and translated (with τ_0) dimensionless time $\tau = \frac{v}{d_{cr}}t + \tau_o$ allows evaluation of data from trains with different speeds on the same plot. Fig. 6c shows the position of the axles of an eastbound Class 185 train on Arch 38 in three instances. At the first instance, $\tau_1 = 3.5$, the front bogie of the leading carriage is above the crown of Arch 38. In the second instance, $\tau_2 = 4.5$, the leading axles have moved one span further. In the third instance, $\tau_3 = 5.35$, the back axle of the leading carriage is above the crown of Arch 38, while

British Rail Class	185	155	144
Wheelbase, bogie centre (m)	16	16	9
Normalised wheelbase	1.9	1.9	1.1
Total length (m)	23.8	23.2	15.1
Typical bogie weight (ton)	33.4	19.2	12.3
Formation (cars)	3	2	4

(a)

(b)

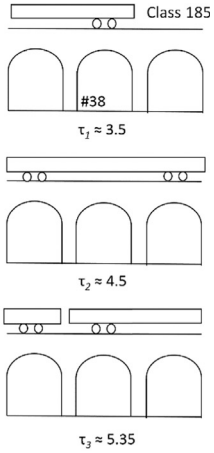

(c)

Fig. 6. (a) A table summarising the relevant characteristic of frequently observed Class 185, 155 and 144 trains on the Leeds-Selby route, alongside (b) their photos, ordered respectively from top to bottom and taken from [29–31] (c) Schematics illustrate the relative location of the axles of a Class 185 train, as it passes over the Arch 38.

Table 2
Properties of the investigated datasets.

Datasets	Date	Camera configuration (see Fig. 4d)	Train model (see Fig. 6)	Direction	Speed (mph)
DS1	07.16	C1	185	E	30.9
DS3	07.16	C2	185	E	31.2
DS9	07.16	C2	185	W	30.0
DS11	01.16	No cameras	185	E	30.9
DS12	07.16	C2	155	E	30.9
DS13	07.16	C1	144	E	29

the front axle of the second carriage is above Arch 37. These instances are repeated cyclically throughout the train passage. Data points at these specific instances are highlighted for discussions throughout the paper. The six datasets investigated and compared in this paper (Table 2) describe the structural response to different trains travelling in different directions.

4. Pier response mechanisms

This section examines the longitudinal and transverse response of the piers during the passage of a Class 185 train. Datasets 1 and 3 (denoted by DS1 and DS3, see Table 2) describe the response to an eastbound train which passes over the northern tracks. In Fig. 7a, the opening and closing of span 38N at the top of the piers (i.e. the relative displacement between monitoring targets WP-EP, denoted by Δ(WP−EP)) is shown. Here, and in the rest of the paper, the positive sign convention of one of the datasets in the graph (the line with highlighted instances) is demonstrated by the inset illustration of a bridge cross-section in the XY plane in accordance with Fig. 6. In this case, positive values of Δ(WP−EP) indicate span opening whereas negative values indicate span closing. The data shows a near-identical response for two similar trains (DS1 and DS3) despite different DIC configurations (C1 and C2, see Fig. 4). This demonstrates the repeatability of data, which has been examined in detail elsewhere [25]. Additionally, the highlighted instances indicate that at $\tau = 3.5$, the axle over the crown of 38N pushes the piers outwards, causing the 38N span to open by about 0.7 mm. At $\tau = 4.5$, the axles located over the crowns of the neighbouring spans push the piers inwards, causing a similar magnitude of span closing. At $\tau = 5.35$, span opening is observed due to an axle located above the crown of 38N. However, the span opening has a reduced magnitude of 0.35 mm, since an axle above the neighbouring pier of 37N does not allow movement of the pier in the direction of X between Arches 37 and 38. These instances are repeated several times during the passage of a train.

Fig. 7b illustrates the span opening and closing in monitoring planes 37N and 38S for DS1 and DS3. All of these signals show a similar characteristic trace. However, the span opening and closing of 37N is offset in time. While a span opening is observed for 38N at $\tau = 3.5$, the pier movements due to axles over Arches 36 & 38 cause span closing in 37N. It is notable that the maximum span opening of 0.6 mm for 37N is smaller than the maximum opening of 0.7 mm for 38N. Similarly, the span opening trace of 38S, located under the southern track, experiences a smaller maximum span opening of 0.3 mm. This indicates a torsional rotation of the pier in the XZ plane between Arches 37 and 38, resulting in larger northern pier top movements in comparison to the south.

Fig. 7c describes the absolute displacement ΔX at the western and eastern pier monitoring targets WP and EP for Arches 37 and 38 for DS1. The western and eastern piers of Arch 38N move in opposite directions to allow span opening at the instance $\tau = 3.5$ although the movements at the damaged western pier are larger in magnitude. Furthermore, at the third highlighted instance $\tau = 5.35$ it can be seen that the target 38N WP moves only slightly in the X direction, due to axles on either side of this pier. Meanwhile, 38N EP moves freely, causing the span opening. In addition, the figure plots the ΔX displacement of 37N EP. This movement of this target is similar to that of 38N WP, which indicates that opposite sides of the same pier move together. The vertical axial strains recorded on the pier between Arches

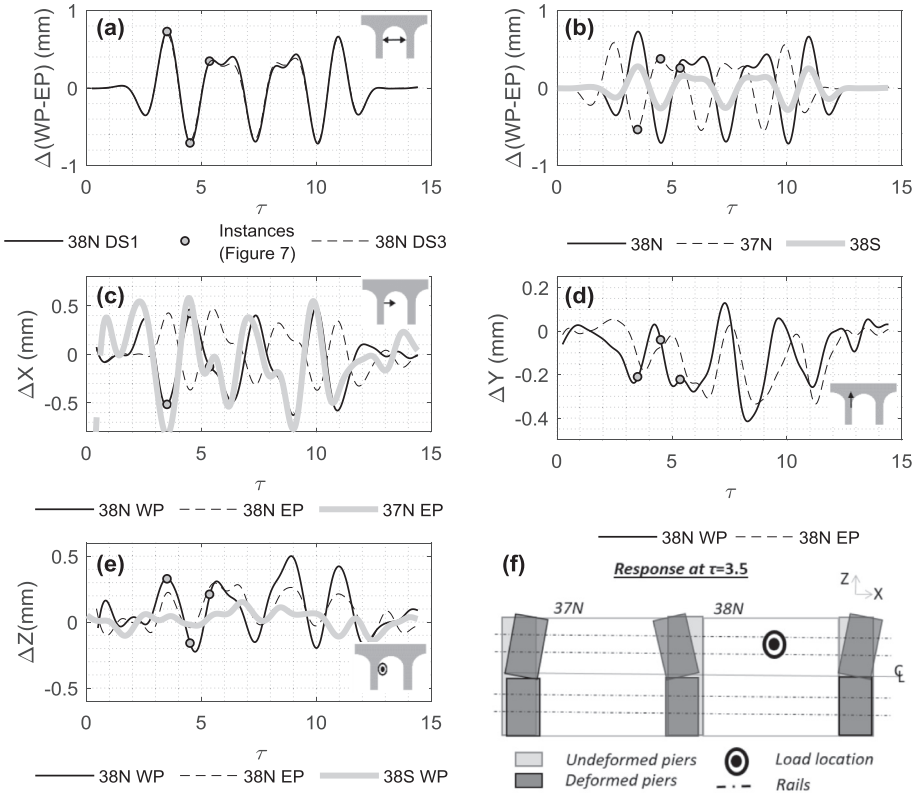

Fig. 7. Pier top displacement time histories from DS1 and DS3 with highlighted instances: (a) 38N span opening from different datasets, (b) comparison of span opening in 38N, 38S and 37N. (c) Horizontal ΔX, (d) vertical ΔY and (e) transverse ΔZ pier movements are also shown. A schematic (f) illustrates the plan view of observed response of pier tops at a specific instant.

37 and 38 were negligibly small (not shown), indicating that these ΔX movements are primarily due to rigid body rotations (e.g. rotations in the XY and XZ planes) of the pier. Fig. 7d describes the vertical movement ΔY at 38N pier tops for DS1, where the highlighted instances are again shown with circular markers. These movements indicate different characteristic traces. Here, the movements are negative, which indicates that the arch is sinking into the ground during the passage of the train. Fig. 7e describes the accompanying transverse movements ΔZ of pier top targets WP and EP, showing that at 38N, the western and eastern piers experience similar noteworthy transverse movements which have a characteristic time history that is similar to the span opening and closing. At the instant, $\tau = 3.5$, a transverse movement of approximately 0.2 mm is observed in the positive Z direction (see the inset illustration and Fig. 5b for the sign conventions). Conversely, at the instance, $\tau = 4.5$, a negative transverse movement occurs in Arch 38N, indicating that the pier rotates towards the relieving arch by a similar amount. The damage due to residual transverse rotation of bricks (in the YZ plane) in the pier between 37N and 38N was highlighted earlier in Fig. 3, and the structural interventions (e.g. concrete filling and ties) which were done to minimise this rotation were noted. The presented results indicate that the 38N pier tops are still rotating in the transverse (YZ) plane in small amounts. The transverse movements of 38S WP are also shown in Fig. 7e, and these are negligible in comparison to the data from the northern portion of the arch during the passage of an eastbound train.

These transverse and longitudinal movements of the piers are summarised in a schematic plan view in Fig. 7f. This view shows the structural response at the instant $\tau = 3.5$ with a load in the northern tracks. In this schematic, each pier is represented as two macro blocks, separated above the relieving arch. Cracking in this area allows the northern part of pier to rotate more than the southern part in the XZ plane, leading to larger span opening on northern side of the relieving arch. In this representation, due to existing damage in the northern spandrel wall (see Fig. 3), the spandrel wall does not restrict pier rotations. Further measurements using DIC (not shown) support this assumption. The influence of these three-dimensional pier movements on the arch response will be examined next.

5. Arch response mechanisms

This section investigates the arch barrel response mechanisms accompanying the pier movements. To do this, Fig. 8a shows the span opening/closing and the vertical crown displacements at A5 from DS1. According to this trace, the crown displaces 1.3 mm downwards at $\tau = 3.5$, while moving up only about 0.55 mm at $\tau = 4.5$. Vertical crown displacements relative to the western springing, denoted by ΔY(A1-A5), are also plotted in Fig. 8a, indicating -1.1 mm and 0.65 mm at the same instances. This 70% magnitude difference between vertical crown displacements is noteworthy, since a similar magnitude of span opening and closing (0.7 mm) is experienced by the piers at these instances. This indicates that different arch mechanisms occur to accommodate opening and closing of the span. This statement is further explored in Fig. 8b, which compares the crown strain response recorded between the clamps located at A4-A5 and the relative vertical displacement between the crown and western springing. Positive and negative strains indicate tension and compression, and appear during span opening and closing, respectively. The characteristic time history response of the two signals in Fig. 8b are remarkably similar; just as in the vertical displacement data, the magnitude of crown tensile strains experienced at $\tau = 3.5$ is 70% larger than the crown compressive strain experienced at $\tau = 4.5$. However, the crown deflections and strains do not always follow the same trend as span opening and closing. At the instant $\tau = 5.35$ the western pier does not move in the X direction, and the span opening at the springing level reduces to 0.35 mm, which is 50% of the span opening of 0.7 mm at $\tau = 3.5$. However, the crown strains and vertical deflections in the instant $\tau = 5.35$ are approximately 80% to those at $\tau = 3.5$. This indicates that a different mechanism also takes place when the span opening is caused only by one of the piers. These mechanisms are examined further with strain and deflection data in the following paragraph.

Fig. 9 shows the longitudinal response from the monitoring plane 38N. Fig. 9a-b show the ΔY and ΔX movements in the western section of the arch barrel. The plots feature data from the monitoring targets at the western springing A1, western quarter span A3 and crown A5. As expected, ΔY movements increase towards the crown while ΔX movements are the highest at the springing and smallest at the crown. These movements could be caused by a combination elastic deformations and rigid body rotations of sections of the arch. In a rigidly rotating body, rotations calculated from displacements in different parts of the structure would be expected to be identical. To investigate the extent to which rigid body rotations can explain the measured response, the XY plane rotation β between the monitoring points was calculated. Fig. 9c-f shows the calculated rotations (schematically shown with inset figures with the positive counter-clockwise sign convention) for DS1. In Fig. 9c, the XY plane rotations in the monitoring plane 38N, for sections just below and above transverse crack, denoted by $\beta_{A1\text{-}A2}$ and $\beta_{A3\text{-}A4}$, are shown. Both rotation traces are negative, but the magnitude of $\beta_{A3\text{-}A4}$ is significantly larger than that of $\beta_{A1\text{-}A2}$ at $\tau = 3.5$. This implies that these sections rotate in the same direction but not as a rigid body. In contrast, when the span is closing at $\tau = 4.5$, $\beta_{A1\text{-}A2}$ and $\beta_{A3\text{-}A4}$ are similar in magnitude and direction, indicating rigid body rotation. The additional rotation in $\beta_{A3\text{-}A4}$ results in higher vertical displacements of the crown during span opening, highlighting the different arch response mechanisms.

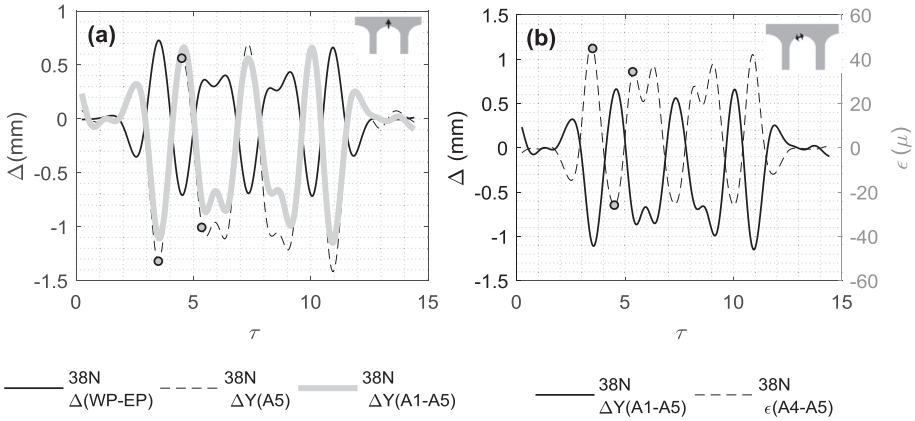

Fig. 8. Longitudinal plane time history response from DS1 for the monitoring plane 38N: (a) Span opening at pier-top and vertical crown displacements (absolute and relative to western springing) and (b) vertical relative displacement and strain at the arch crown.

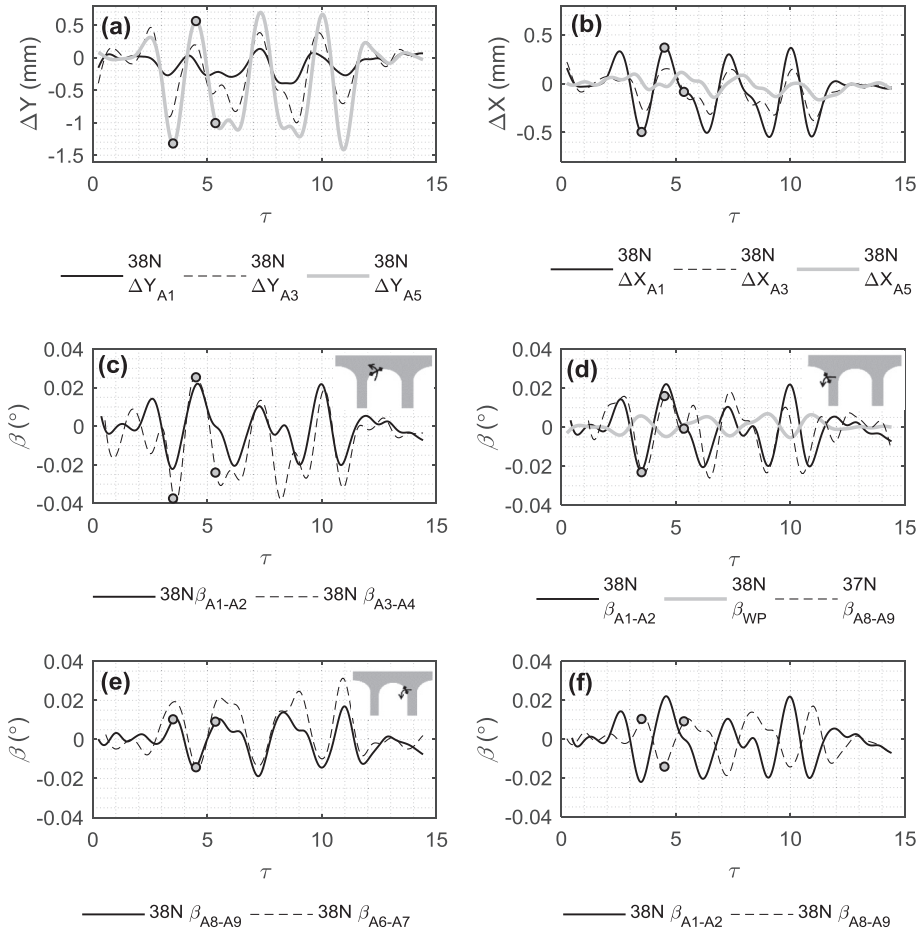

Fig. 9. Longitudinal plane time history response from DS1 for the monitoring plane 38N: (a) Vertical ΔY and (b) horizontal ΔX movements at the western springing, quarter span and crown. (c–f) The in-plane (XY plane) rotations calculated from these displacements are shown and are used to compare in-plane rotations at different sections of the piers and arches of 37N and 38N.

Another important aspect of response can also be seen by noting the rotations at the instant $\tau = 5.35$ in Fig. 9c. At this instant, the magnitude of $\beta_{A1\text{-}A2}$ is close to zero as the pier between Arches 37 and 38 does not move in the X direction, holding the arch and backing in place. However, at this time, significant rotations are observed for $\beta_{A3\text{-}A4}$. This rotation is enabled by the open transverse crack between monitoring targets A2 and A3 (see Fig. 3). The closing of this transverse crack due to dynamic loading contributes to the differential rotation between the aforementioned sections. This observation will be further supported with strain data later. In addition, Fig. 9d shows the calculated rotations on either side of the pier shared by Arches 37 and 38. These rotations are $\beta_{A1\text{-}A2}$ from the monitoring plane 38N and $\beta_{A8\text{-}A9}$ rom the monitoring plane 37N. These rotations are remarkably similar, indicating that the portions of both arches near their springing rotate together with the backing, in the opposite direction to the rotation of the pier, approximated as a rigid body rotation, denoted by β_{WP}. The corresponding data was examined for the eastern side of the arch for the same monitoring plane 38N. The ΔY and ΔX displacements along the eastern side of the arch (not shown) demonstrated similar trends as the western side. However, the XY plane rotation data shows an interesting difference. In Fig. 9e, $\beta_{A6\text{-}A7}$ and $\beta_{A8\text{-}A9}$ indicate similar magnitudes of rotation, with less obvious distinction between positive and negative rotations compared to the western side. This could be explained by the lack of an open transverse crack on the eastern side of the arch.

The observations from the rotation data are supported further by the strain data of DS1 for Arch 38 in Fig. 10. The top row shows data from the western portion of 38N, while the bottom row shows data from the eastern portion. It is critical to note that the highest magnitude strains are observed between locations A2-A3. In particular, a maximum strain of 220 $\mu\varepsilon$ is observed just after $\tau = 5.35$. This corresponds to the considerable differential rotation that was observed between $\beta_{A1\text{-}A2}$ and $\beta_{A3\text{-}A4}$ in Fig. 9c. It is noteworthy that this maximum strain value is an order of magnitude larger than all other strains in 38N and clearly indicates the closing of an open crack (see Fig. 3 for a photo of this crack). This area never experiences tensile strains. At the symmetric location on the east side of the arch, the segment A7-A8 experiences compressive strains smaller than 60 $\mu\varepsilon$ at any one time, as there is no open crack present in this region. This is consistent with the rotation data in Fig. 9e. The crown segments A3-A4, A4-A5 and A5-A6 are the longitudinal segments which experience tensile strains during span opening. For these locations, the strain magnitude peaks at approximately 50 $\mu\varepsilon$ at around $\tau = 3.5$. The other crown sensor between A6-A7 experiences lesser tensile strains, and appears to be shifted. From this data, it is clear that the longitudinal plane tensile strains which emerge during span opening are more distributed, with little indication of strain localisation. In addition, a slight asymmetry of the response due to the presence of the transverse crack on the western part of the span can also be noted since the tensile strain concentrates more towards the west of the crown.

In the previous paragraphs, the arch barrel data from under the loaded northern tracks have been investigated. For the same train loading, it is necessary to investigate the arch longitudinal response in the south. Fig. 11 shows the key longitudinal response time histories from the monitoring plane 38S and compares them to the equivalent quantities in 38N. DS3 is used for this purpose. In Fig. 11a, the span opening data for 38S and 38N demonstrate the same characteristic trace, although the span opening magnitude in the south is one-half of the magnitude in the north. A more drastic reduction is observed for the vertical crown displacements; displacements in 38N are three to four times higher than the displacements in 38S (Fig. 11b). A similar level of decrease from 38N to 38S is observed for the strains and in-plane rotations in Fig. 11c and d. This demonstrates the effective concentration

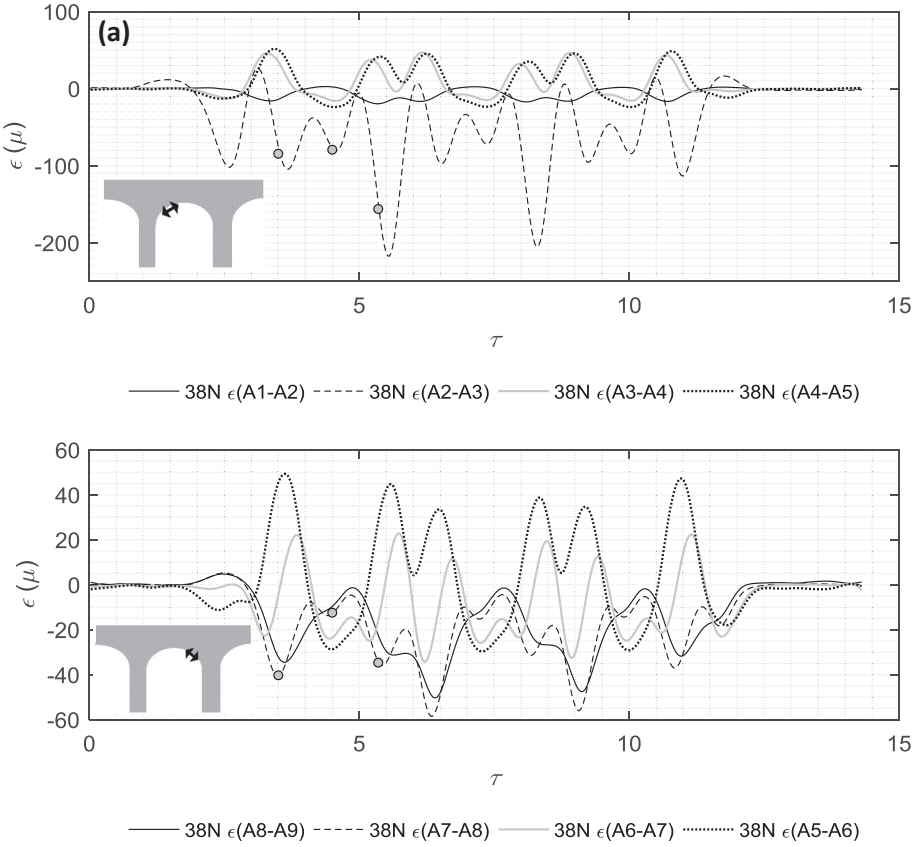

Fig. 10. Longitudinal plane strain time history response from DS1 for 38N: Data from the (a) western and (b) eastern fibre optic segments.

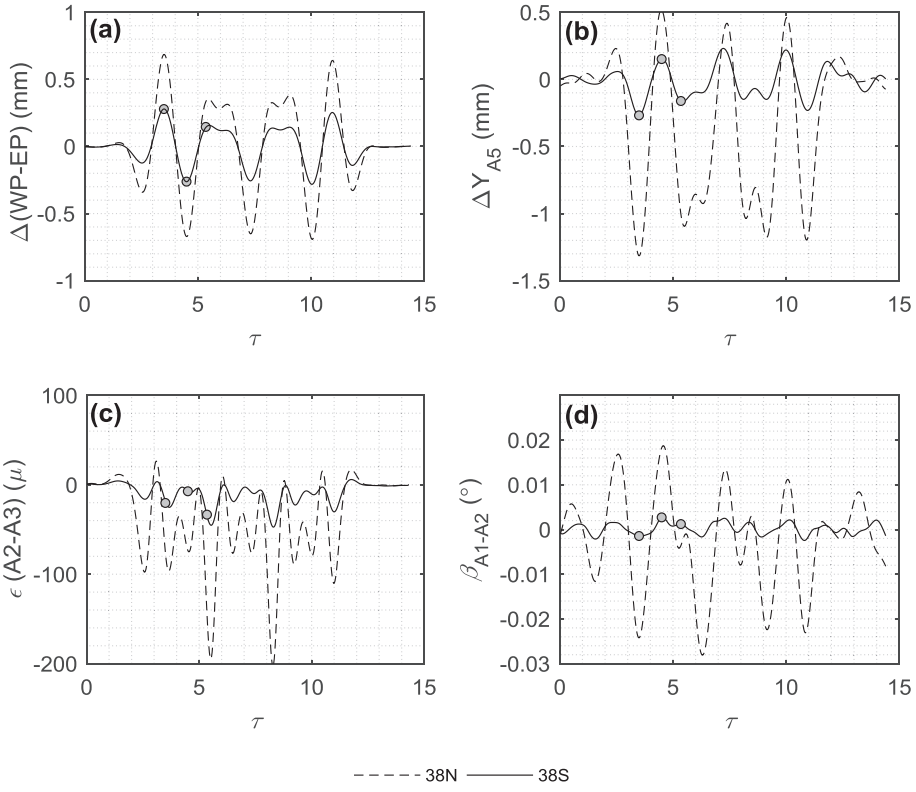

Fig. 11. Longitudinal plane time history response from DS3 for the monitoring planes 38S and 38N: (Top left) Span opening at pier-top, (top right) vertical displacements at the crown, (bottom left) strain in the lower quarter-span region and (bottom right) in-plane rotation between springing and quarter span.

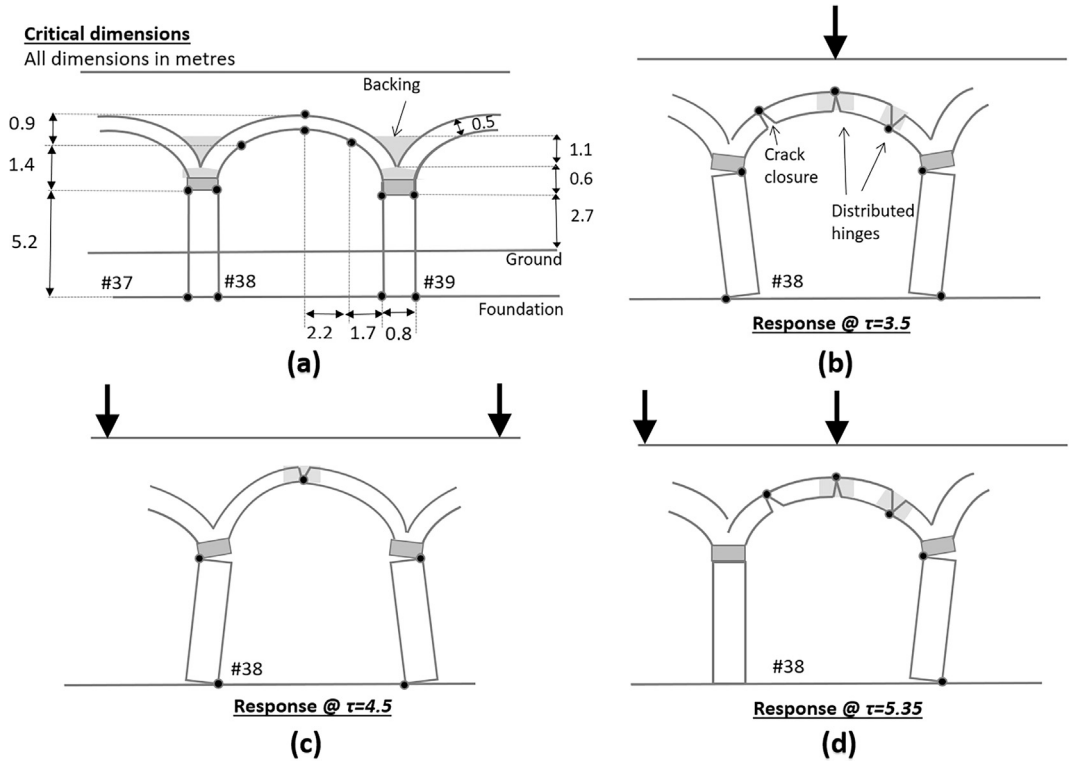

Fig. 12. (a) Dimensions for a simple rigid body model with highlighted hinges proposed to approximate behaviour and (b–d) a schematic representation of the model response to axle loading in different locations.

of response in the northern and more damaged half of the arch.

On the basis of these findings, Fig. 12 proposes a simple model to summarise the fundamental aspects of the longitudinal response. On top left of this figure, the proposed hinge locations and distances between these hinges are shown. Then, for each of the highlighted instances in Fig. 6, the behaviour is illustrated with the simple model. Note that the "hinges" are only representative of where strain tends to concentrate and how the bridge tends to deform, but are not meant to suggest that only rigid body rotations take place, or that elastic deformations are insignificant. At $\tau = 3.5$, where the axle is above the crown, the piers are pushed outwards due to increased thrust in X direction, which causes pier rotation in the XY plane about pier foundations. The foundation hinges depicted in the figure are representative of a rotation point or region somewhere at or beneath the ground surface level; a distinct hinge could not be identified. To accommodate the span movement, four intrados hinges form. Two of these are located just under the skewback stones, where crack opening does seem to concentrate in distinct joints, and allows the backing to rotate together with two arches on its sides. In addition, two intrados hinges form just above the backing area. Here, significant rotation towards the bridge centreline was observed for the western intrados hinge (see Fig. 9c), so this "hinge" is actually manifest in closing of the intrados crack at this location. The symmetric eastern intrados hinge is not discrete but is representative of the increase of compressive strain in this region. This likely involves significant bending deformation, and involves relatively small local rotations (see Fig. 9e). Together, the two intrados hinges cause the crown to depress significantly and experience tensile strains on the intrados. In reality, these tensile strains at the crown are distributed and do not concentrate around an extrados hinge (see Fig. 10).

At $\tau = 4.5$, the data indicated a different mechanism with smaller displacements. This mechanism is a simple span closing mechanism, with hinges under the skewbacks and an intrados hinge at the arch crown. Again, the skewback hinges are discrete, while the crown hinge is representative of distributed compressive strain at the arch intrados. The consistent rotations of segments of the arch (see Fig. 9c and e) indicate that the span closing mechanism involves rotation of half of the arch as a whole unit. Finally, at $\tau = 5.35$ the span opening is due to the ΔX movement of the eastern pier. Since the skewback hinge on the western side of the pier is not activated for this particular case, almost all the rotation occurs around the western intrados hinge point located at approximately the backing height. The data captures the localisation of strains and rotations about this hinge point. In short, Fig. 12 demonstrates the longitudinal response mechanisms, for different scenarios. Similar mechanisms are observed on all sections of Arches 37 and 38, although the magnitude of span opening, and the concentration of strain and rotations due to cracks, varies. The hinge locations indicated in these models represent areas where future degradation may be expected. There are other areas of potential damage, which stem from the transverse response mechanisms which are discussed next.

To determine the transverse arch response mechanisms, displacement and strain data from DS1 and DS2 will be primarily utilised. Fig. 13a compares the transverse (Z-direction) movements at the crown of the arch with transverse movement at the western pier top for 38N and 38S. Here, it can be observed that the crown transverse movements in both 38N and 38S are significantly smaller than the pier transverse movements and can be neglected. These measurements hint at a rotation mechanism in the XZ plane, where the arch barrel moves away from the bridge centreline at the springing. This indicates that at $\tau = 3.5$, the existing longitudinal crack above the relieving arch at the springing level opens due to the northward movement of the western springing. The observation of cracking in this area was discussed earlier and shown in Fig. 3 and will be further examined with strain data.

Fig. 13b shows the first three strain measurements from the monitoring plane 38W, which are placed in the northern half of the structure. All of these measurements show tensile transverse bending strain that is induced when the axles are on the investigated span (e.g. at $\tau = 3.5$ and $\tau = 5.35$). At $\tau = 4.5$, there is no axle above Arch 38, and minor compressive strains are observed. The measurement ε(T2-T3) is taken directly under the tracks and experiences the highest strains. In Fig. 13c, the three transverse measurements from the southern section

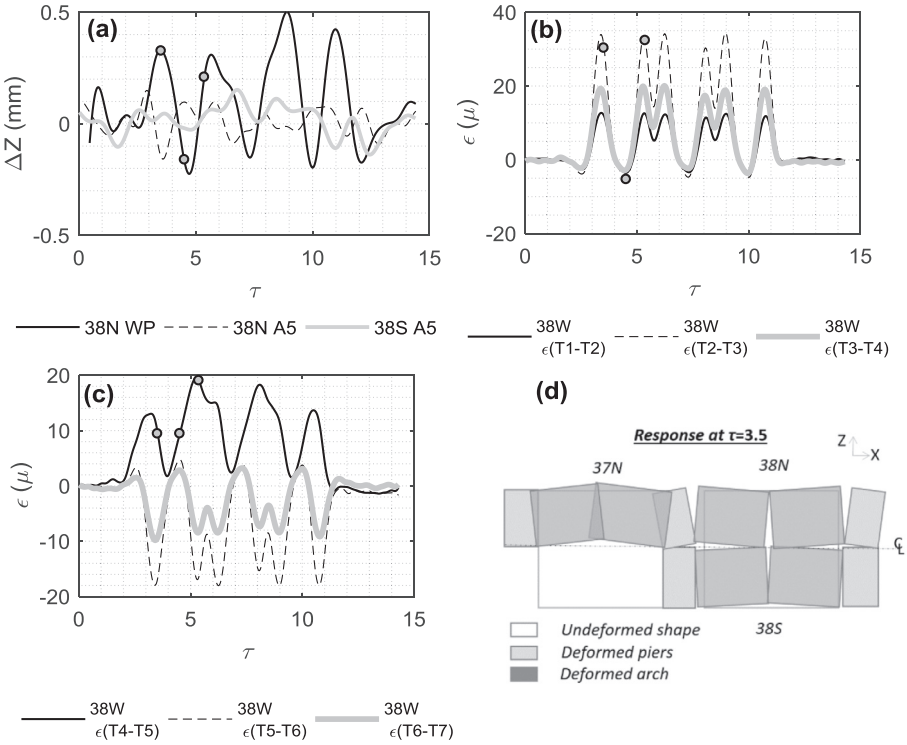

Fig. 13. Time history response from DS1 and DS2 to describe the transverse behaviour of the arch: (a) A comparison of pier top and arch crown transverse ΔZ pier displacements, strain data from (b) northern and (c) southern fibre optic segments of transverse monitoring plane 38W. A plan view schematic (d) illustrates the observed transverse response of arches at $\tau = 3.5$.

of 38W are shown. As expected, the measurements ε(T5-T6) and ε(T6-T7) show negative compressive strains, indicative of a hogging moment. This behaviour is typical of 3D arch membrane behaviour and has been discussed in numerous works in the literature [26,27]. However, the ε(T4-T5) signal is unusual, displaying less well-defined peaks and indicating tensile strain at $\tau = 4.5$. The unusual behaviour of this section is likely to be due to its location over a hairline longitudinal crack. As opposed to other sections which measure the bending strains, this section measures the opening and closing of the crack as well.

Fig. 13d summarises the indicated transverse response mechanism of the arches at the instance $\tau = 3.5$ with a schematic plan view drawing. In this drawing, the response of the arches is sketched over deformed piers, which were previously shown in Fig. 7. This schematic illustrates the transverse movement of components by dividing the arches and piers into macro blocks. The northwest macro block of Arch 38 transmits the vertical loads from a train axle in the midspan of Arch 38 through a concentrated area near the relieving arch. This concentration allows loss of contact at the exterior edge, allowing the skewback to rotate in the XZ plane as it is supported primarily on its interior edge. The northwest macro block of Arch 38 also rotates in the XZ plane to allow the springing of the northwest macro block to move northwards (positive Z direction). This behaviour causes the longitudinal crack above the relieving arch to open. In the schematic, the concentration of movements in the northern part of these arches and their observed interaction are highlighted.

6. Pier & arch response to different loads

This section investigates the salient aspects of the pier and arch response to different loads. Within this context, the span opening and closing of the piers, the vertical deflections and strains at the crown, strains over the transverse and longitudinal crack and the XY plane rotation at the springing are examined.

Fig. 14 shows the longitudinal response of the monitoring planes 38S and 38N to a westbound train (DS9) which travels on the southern tracks above 38S. Comparing the results from this figure to Fig. 11, where the longitudinal response of the same planes to the eastbound Class 185 train was examined, is useful. According to Fig. 14a, the maximum span opening experienced at 38S in the instance $\tau = 3.5$ is only 0.45 mm, as opposed to the movement of 0.7 mm experienced by 38N when the train was on the other track (Fig. 11). However, the span opening experienced at 38N in the instance $\tau = 3.5$ is 0.25 mm, which is similar to the movement of 0.3 mm experienced by 38S in Fig. 14. The vertical displacement traces in Fig. 14b for the crown indicate a similar phenomenon. A maximum vertical displacement of 0.75 mm is experienced at this location in 38S. However, when the train is on the northern tracks 38N experiences 1.3 mm of vertical deflection. Fig. 14c shows the axial strains between A2-A3, just above the backing, for 38S. High levels of strain are observed in 38S, though the maximum value reduced to 100 $\mu\varepsilon$ compared to the maximum of 200 $\mu\varepsilon$ observed in Fig. 11c for 38N. Finally, Fig. 14d shows the rotation of the western springing $\beta_{A1\text{-}A2}$ for 38S and 38N. The rotation behaviour for the westbound train is qualitatively similar to the rotation behaviour observed for the eastbound train in Fig. 11d, and the relative difference between 38N and 38S in Fig. 14d is again smaller than that shown in Fig. 11d. These results consistently indicate that relative movements between the north and the south sections are not proportional. Local aspects, such as the distribution of damage in the arch and the pier or the soil conditions underneath the structure, cause this dissimilar response, and concentrate the response in the northern part of the arch.

As mentioned earlier, data was gathered during two site visits. During the first site visit in January 2016, FBG data was gathered from Arch 37. The sensors were left in place for six months, and data was collected again from Arch 37 during the second visit in July 2016. Fig. 15 shows that the span opening, crown strain, quarter span strain and transverse strain over the longitudinal crack are very similar in both datasets. Although a temperature difference of around 15 degrees existed between the two dates, dynamic strain measurements varied a maximum of 15 $\mu\varepsilon$. This level of strain difference is not dissimilar to the small strain differences observed due to the live loads in trains [25]. This indicates that the response varied little during this time, without any significant change in behaviour.

Fig. 16 describes the response of monitoring plane 38N to an eastbound Class 155 train and contrasts it to the response to a Class 185

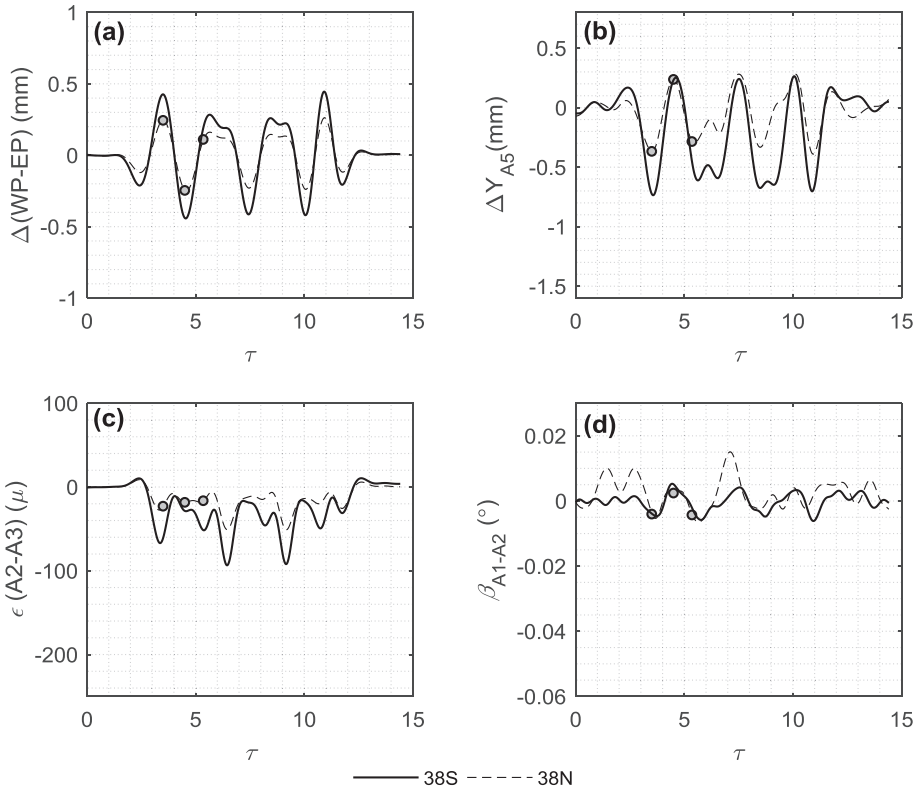

Fig. 14. Time history response from DS9 for the monitoring planes 38S and 38N: (Top left) Span opening at pier-top, (top right) vertical displacements at the crown, (bottom left) strain in the lower quarter-span region and (bottom right) in-plane rotation between springing and quarter span. As opposed to previous datasets, the train travels on the southern track in the opposite (west) direction for this dataset.

train. Fig. 6 described the characteristics of these vehicles, highlighting that the dimensions of each car Class 155 and 185 trains are very similar. However, the investigated Class 155 train is composed of two cars instead of three, and is 40% lighter. The response signature described by Fig. 16 is largely governed by the axle positions and therefore the characteristic response trace to these two vehicles are very similar. However, due its lower weight Class 155 causes smaller span opening (0.5 mm versus 0.7 mm at $\tau = 3.5$), crown vertical displacements (1mm versus 1.3 mm at $\tau = 3.5$), strains and rotations (see Fig. 16c and d). As opposed to Class 155 and 185 trains, Class 144 trains

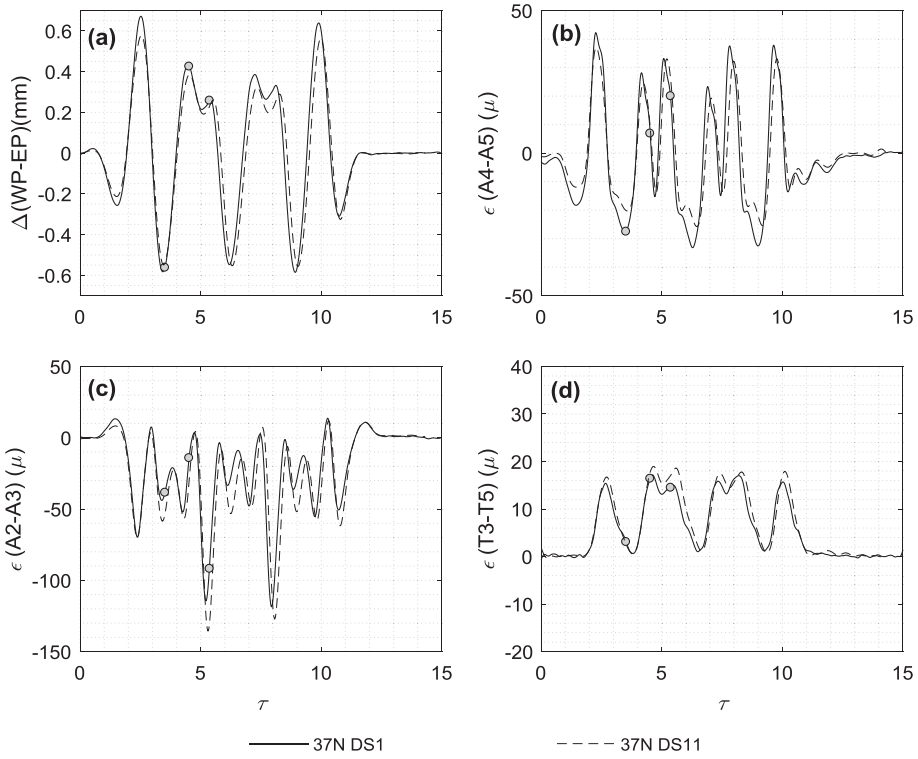

Fig. 15. Time history responses from DS1 and DS11 for the monitoring plane 37N: (a) Span opening at pier-top, (b) strain at the crown region, (c) strain in the lower quarter-span region and (d) transverse strain over the longitudinal crack on the eastern portion of the arch. DS1 and DS11 were recorded six months apart.

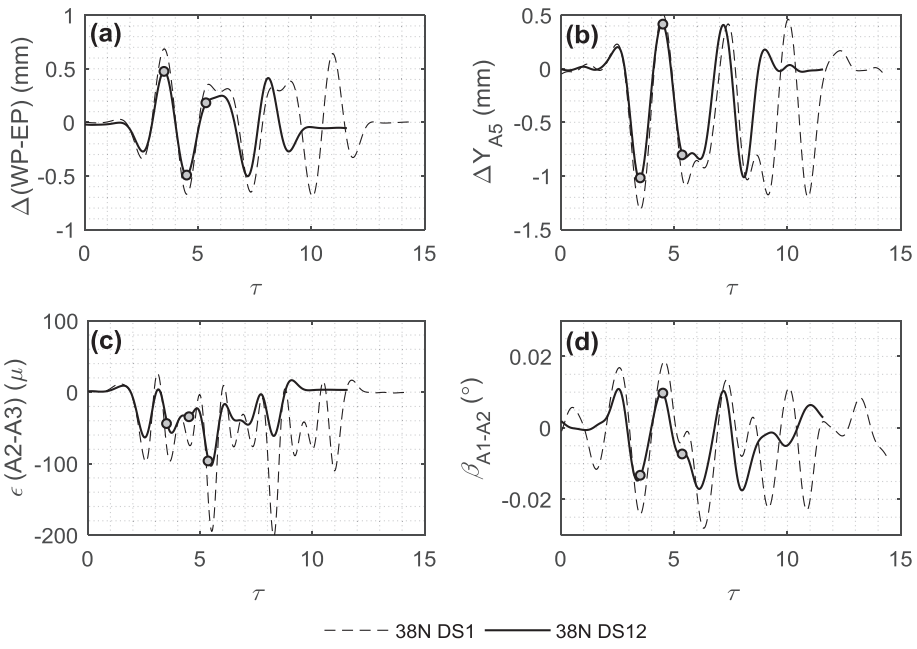

Fig. 16. Time history response from DS1 and DS12 for the monitoring plane 38N: (a) Span opening at pier-top, (b) vertical displacements at the crown, (c) strain in the lower quarter-span region and (c) in-plane arch rotation above the springing. DS1 records response to a three car Class 185 train, while the DS12 examines the response to a two car Class 155 train.

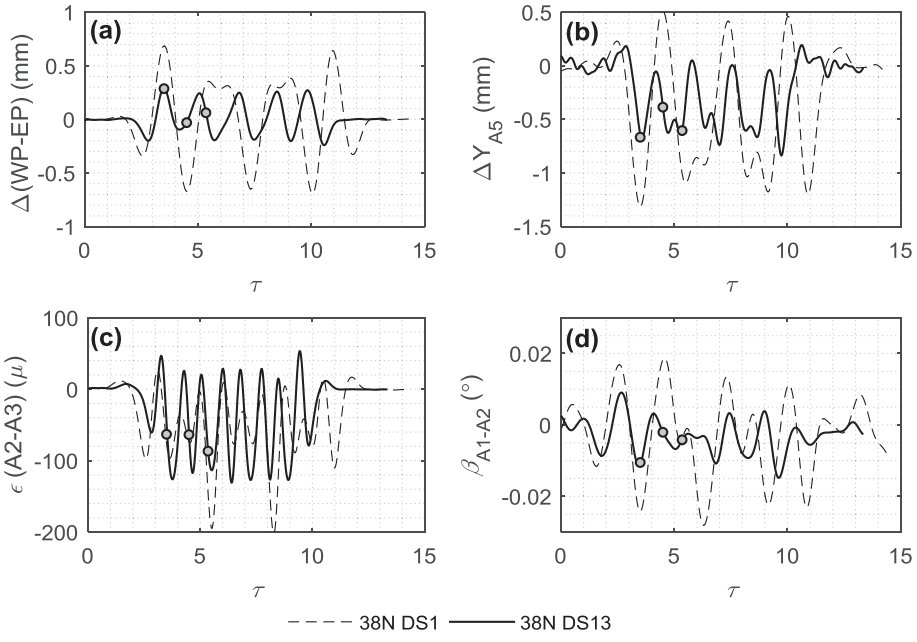

Fig. 17. Time history response from DS1 and DS13 for the monitoring plane 38N: (a) Span opening at pier-top, (b) vertical displacements at the crown, (c) strain in the lower quarter-span region and (d) in-plane arch rotation above the springing. DS 1 records response to a three car Class 185 train, while the DS12 examines the response to a four car Class 144 train.

have a shorter wheelbase, which approximately equals to the span. Therefore at each of the instances τ = 3.5,4.5,5.35 shown in Fig. 6, there would be an axle above the crown of Arch 38. Fig. 17a shows the span opening response pattern for a Class 144 train. The characteristic trace of Class 185 and 155 trains is replaced by higher frequency cycles, where the span opening is prominent and span closing is reduced. It is also interesting that the highest span opening is observed at the instance τ = 3.5 where the leading carriage axles are placed above the crowns of Arches 37 and 38. In contrast, at the instances τ = 4.5,5.35, the span opening is close to zero, as the axles above spans 37, 38 and 39 limit pier movements.

Fig. 17b demonstrates that the crown vertical displacements are predominantly negative for Class 144 trains. This is due to the narrow wheelbase of Class 144 trains which prevent pure closing of unloaded spans. Furthermore, despite negligible span opening at the instances τ = 4.5,5.35, vertical displacements close to 0.5 mm are experienced at both instances. This suggests that the section of the arch above the backing is deforming in flexure, to allow these movements. A similar behaviour was noted earlier for Class 185 train at τ = 5.35 in Fig. 12d. Fig. 17c and d present evidence of this rotation behaviour in the arch. The strain above the backing area, ε(A2-A3) remains consistently high, and is close to its maximum value in the instances τ = 4.5,5.35 where the arch is flexing. The strains experienced in this location are an order of magnitude higher than strains experienced elsewhere. The maximum strain of 130 $\mu\varepsilon$ is less than Class 185 train response strain of 200 $\mu\varepsilon$. However, this represents a noteworthy increase in strain concentration when it is noted that the weight of the Class 144 bogie is 40% of the weight of the Class 185 bogie. In addition, the rotation trace in Fig. 17d reinforces these observations. The rotations experienced at the instances τ = 4.5,5.35 are small, as the pier cannot rotate. This causes significant rotations to accumulate in the arch itself.

7. Discussion and conclusions

This paper presented an investigation of the dynamic behaviour of a brick masonry viaduct with innovative FBG and DIC sensing techniques. The quasi-distributed nature of data allowed extensive measurements of displacements, rotations and strains at many different parts of the bridge. Such extensive measurements provided unique data which enabled new insight into the behaviour. Primarily, the measurements were used to determine the longitudinal and transverse response mechanisms of different components of the viaduct. Correlations and distinctions between different measurements were used to propose critical mechanisms, which were utilised to evaluate and interpret visually observed damage. The data highlighted the following novel aspects concerning dynamic viaduct behaviour:

- The arch behaviour was three-dimensional, particularly due to the relieving arches in the piers. Transverse response, just like longitudinal response mechanisms, can be important to measure.
- Rigid body pier rotations, likely influenced by the soil-structure interaction effects, plays a critical role. Span opening induced large vertical displacements in the arch barrel, while pier torsion interacted with transverse movements and longitudinal cracking in the arch and piers.
- As well as the rigid body rotation of the backing and lower parts of the arch, flexing of the arch above its backing was observed. In particular, trains with a wide wheelbase caused large span opening and predominant rigid body rotation of the arches with their backing. Trains with a narrow wheelbase primarily caused bending within the arch; this type of loading caused only small span opening and rotation at backing level.
- The response of the arch was strongly affected by existing damage. The transverse cracks resulted in a strong localisation of strains, and a modification of the longitudinal response mechanisms.

These results have important implications for improving the existing assessment techniques for masonry viaducts.

- It remains a formidable task to identify existing damage, to understand its progression and its influence on the global behaviour of the structure. Quasi-distributed sensing techniques demonstrated in this paper provide important detail for this purpose and can provide valuable input for serviceability assessments and design of strengthening schemes.
- The train wheelbase was shown to influence the governing modes of viaduct. Commonly used load models such as the Type RA1 loading [28] do not consider the wheelbase as an important factor, but should do so.

Acknowledgements

The work carried out was funded by EPSRC and Innovate UK, through the Cambridge Centre for Smart Infrastructure and Construction (Grant Reference Number EP/L010917/1). The research materials supporting this publication can be accessed at https://doi.org/10.17863/CAM.22572. The authors would like to thank Jason Shardelow, Peter Knott, Giuseppe Narciso, Melanie Banes, Hesham Aldaikh, and Gilly Donaldson for their help in data collection. In addition, the authors are grateful to Mark Norman of Network Rail for his support.

References

[1] Eurostat. Energy, transport and environment indicators. Luxembourg: Publications Office of the European Union; 2016. http://dx.doi.org/10.2785/138586.
[2] Network Rail. Network RUS: Passenger Rolling Stock; 2011.
[3] Orban Z. Assessment, reliability and maintenance of masonry. In: Roca P, Molins C, editors. Arch Bridg. IV-Advances Assessment, Struct. Des. Constr., Barcelona; 2004. p. 152–61.
[4] Sarhosis V, De Santis S, de Felice G. A review of experimental investigations and assessment methods for masonry arch bridges. Struct Infrastruct Eng 2016;12:1439–64.
[5] Harvey WJ, Smith FW. The behaviour and assessment of multispan arches. Struct Eng 1991;69:411–7.
[6] Gilbert M, Melbourne C. Rigid-block analysis of masonry structures. Struct Eng 1994;72:356–61.
[7] Harvey B. Stiffness and damage in masonry bridges. Proc ICE – Bridg Eng 2012;165:127–34.
[8] Melbourne C, Gilbert M. The behaviour of multiring brickwork arch bridges. Struct Eng 1995;73:39–47.
[9] Fanning PJ, Boothby TE, Roberts BJ. Longitudinal and transverse effects in masonry arch assessment. Constr Build Mater 2001;15:51–60.
[10] McKibbins LD, Melbourne C, Sawar N, Gaillard CS. CIRIA C656: Masonry arch bridges: condition appraisal and remedial treatment. London; 2006.
[11] Orbán Z, Gutermann M. Assessment of masonry arch railway bridges using non-destructive in-situ testing methods. Eng Struct 2009;31:2287–98.
[12] Forde MC. International practice using NDE for the inspection of concrete and masonry arch bridges. Bridg Struct 2010;6:25–34.
[13] Conde B, Drosopoulos GA, Stavroulakis GE, Riveiro B, Stavroulaki ME. Inverse analysis of masonry arch bridges for damaged condition investigation: application on Kakodiki bridge. Eng Struct 2016;127:388–401.
[14] Acikgoz S, Soga K, Woodhams J. Evaluation of the response of a vaulted masonry structure to differential settlements using point cloud data and limit analyses. Constr Build Mater 2017;150:916–31.
[15] Ye C, Riley E, Pendrigh S, Acikgoz S, DeJong M. Detection of masonry arch bridge historic deformations using point cloud data; 2017.
[16] Kishen JMC, Ramaswamy A, Manohar CS. Safety assessment of a masonry arch bridge: field testing and simulations. J Bridg Eng 2013;18:162–71.
[17] Brookes C. Pop bottle bridge supplementary load test. Southampton, UK; 2004.
[18] Domede N, Sellier A, Stablon T. Structural analysis of a multi-span railway masonry bridge combining in situ observations, laboratory tests and damage modelling. Eng Struct 2013;56:837–49.
[19] Fanning P, Boothby T. Three-dimensional modelling and full-scale testing of stone arch bridges. Comput Struct 2001;79:2645–62.
[20] Brencich A, Sabia D. Experimental identification of a multi-span masonry bridge: the Tanaro Bridge. Constr Build Mater 2008;22:2087–99.
[21] Acikgoz S, Pelecanos L, Giardina G, Aitken J, Soga K. Distributed sensing of a masonry vault during nearby piling. Struct Control Heal Monit 2016;24.
[22] Hoole K. A Regional History of the Railways of Great Britain, Volume 4: The North East. Newton Abbot, David and Charles; 1973.
[23] Harvey B, Harvey H. On the service behaviour of masonry viaducts. Proc ICE – Bridg Eng 2017. http://dx.doi.org/10.1680/jbren.15.00031.
[24] Majumder M, Gangopadhyay TK, Chakraborty AK, Dasgupta K, Bhattacharya DK. Fibre Bragg gratings in structural health monitoring-present status and applications. Sens Actuators, A Phys 2008;147:150–64.
[25] Acikgoz S, DeJong MJ, Soga K. Sensing dynamic displacements in masonry rail bridges using 2D digital image correlation; 2017.
[26] Chettoe CS, Henderson W. Masonry arch bridges: a study. Proc Inst Civ Eng 1957;7:723–74.
[27] Davey N. Tests on Road Bridges, National Building Studies Research Paper No. 16. London, UK; 1953.
[28] Network Rail. NR/GN/CIV/025: The structural assessment of underbridges. London; 2006.
[29] https://en.wikipedia.org/wiki/British_Rail_Class_185.
[30] https://en.wikipedia.org/wiki/British_Rail_Class_155.
[31] https://en.wikipedia.org/wiki/British_Rail_Class_144.